Intertwined charge, spin, and orbital degrees of freedom under electronic correlations in the one-dimensional Fe^{3+} chalcogenide chain

Yang Zhang [1,2] Pontus Laurell [3,4] Gonzalo Alvarez [5] Adriana Moreo [1,2] Thomas A. Maier [5] Ling-Fang Lin [1,*] and Elbio Dagotto [1,2,†]

[1]*Department of Physics and Astronomy, University of Tennessee, Knoxville, Tennessee 37996, USA*
[2]*Materials Science and Technology Division, Oak Ridge National Laboratory, Oak Ridge, Tennessee 37831, USA*
[3]*Department of Physics and Astronomy, University of Missouri, Columbia, Missouri 65211, USA*
[4]*Materials Science and Engineering Institute, University of Missouri, Columbia, Missouri 65211, USA*
[5]*Computational Sciences and Engineering Division, Oak Ridge National Laboratory, Oak Ridge, Tennessee 37831, USA*

(Received 13 July 2025; revised 23 April 2026; accepted 20 May 2026; published 9 June 2026)

Motivated by recent developments in the study of quasi-one-dimensional iron systems with Fe^{2+}, we comprehensively study an Fe^{3+} chalcogenide chain system. Based on first-principles calculations, the Fe^{3+} chain has a similar electronic structure to that discussed before for the Fe^{2+} chain, because of the similar FeX_4 (X = S or Se) tetrahedron-chain geometry. Furthermore, a three-orbital electronic Hubbard model for this chain was constructed using the density matrix renormalization group method. A robust antiferromagnetic coupling was unveiled in the chain direction. In addition, in the intermediate electronic correlation U/W region, we found an interesting orbital-selective Mott phase with the coexistence of localized and itinerant electrons (U is the on-site Hubbard repulsion, while W is the electronic bandwidth) based on the orbital-selective behavior observed in the charge fluctuations. Furthermore, we do not observe any obvious pairing tendency in the Fe^{3+} chain in the electronic-correlation U/W region, where superconducting pairing tendencies were reported before in iron ladders. This suggests that superconductivity is unlikely to emerge in the Fe^{3+} systems. Our results clearly establish the similarities and differences between $Fe^{2+}$and Fe^{3+} iron chains, as well as iron ladders.

DOI: 10.1103/th25-rvx7

I. INTRODUCTION

The discovery of pressure-induced superconductivity in the two-leg ladder compounds $BaFe_2S_3$ [1] and $BaFe_2Se_3$ [2], both with $3d^6$ configuration, has attracted intense interest in the iron chalcogenides with a quasi-one-dimensional (Q1D) lattice structure. This discovery has rapidly developed into another exciting new branch of research on iron-based superconductors [3–12]. In those two-leg ladder systems, the interplay among charge, spin, orbital, and lattice degrees of freedom in a reduced dimensional phase space, induces many interesting phenomena such as orbital-selective magnetism [13,14], spin block states [15,16], ferroelectricity [17,18], orbital-selective Mott phases (OSMP) [19–23], insulator–metal transitions under pressure [24,25], as well as orbital order [26]. Motivated by these intriguing discoveries in two-leg ladder systems, a natural question arises: Can iron chains, with similar FeX_4 (X = S or Se) tetrahedron structures, also display similar physical properties and exotic electronic phases?

To our best knowledge, unlike the well-discussed iron ladders, the study of iron chains is still in its early stages. Several iron chalcogenide chains, with different electronic densities, have already been synthesized, such as $BaFe_2X_4$ (X = S, Se) [27,28], $Ce_2O_2FeSe_2$ [29,30], and $AFeX_2$ (A = K, Rb, Cs, and Tl, X = S or Se) [31–34]. Their crystal structures are displayed in Fig. 1. Although these iron-chain compounds crystallize in different space groups, they all share a common structural character: 1D FeX_2 (X = S or Se) chains built from edge-sharing FeX_4 (X = S or Se) tetrahedron blocks, as shown in Fig. 1(b).

The $BaFe_2X_4$ (X = S, Se) family is a typical iron chain with Fe^{3+} [27,28], corresponding to the electronic configuration of iron $3d^5$, and crystallizes in the I4/m crystal structure (No. 87), as shown in Fig. 1(a). A recent neutron experiment revealed a strong antiferromagnetic (AFM) coupling along the chain direction (c axis) and a small ferromagnetic(FM) canting along the b axis [36]. The Fe^{2+} material $Ce_2O_2FeSe_2$ ($3d^6$) has an Ibam crystal structure, which is structurally related to the iron-based superconductor LaFeAsO, as shown in Fig. 1(c). Interestingly, $Ce_2O_2FeSe_2$ displays a FM coupling along the chain direction [29,30]. The origin of the FM order along the chains in $Ce_2O_2FeSe_2$ can be explained by a novel "half-full" mechanism involving the large entanglement between half-filled and fully occupied orbitals proposed by L.-F. Lin *et al*. [37]. In addition, an interesting FM OSMP with both localized and itinerant electrons has also been discussed in the presence of electronic correlations under crystal-field splitting and doping effects [38,39] by using the many-body density matrix renormalization group (DMRG) technique.

The $AFeX_2$ (A = K, Rb, Cs, and Tl and X = S or Se) family is also an Fe^{3+} chain system, with electronic density $3d^5$. They have the same chemical formula but different space groups [31,40–42], as displayed in Figs. 1(d)–1(f). Neutron

*Contact author: lflin@utk.edu
†Contact author: edagotto@utk.edu

 ©2026 American Physical Society

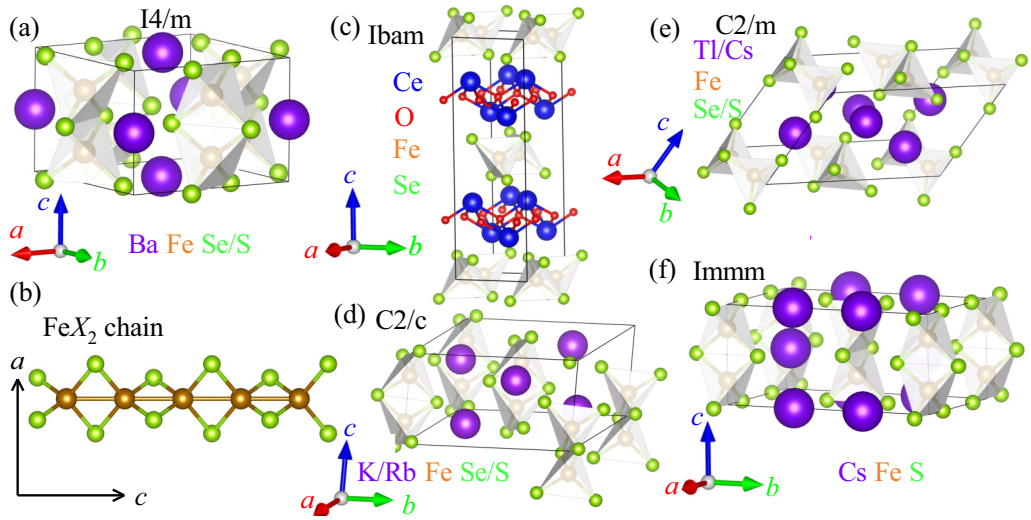

FIG. 1. (a) Schematic crystal structure of $BaFe_2X_4$ (X = S or Se) with space group I4/m (No. 87) in the conventional cell (purple, Ba; brown, Fe; green, Se or S). (b) Sketch of the *ac* plane viewed along the iron-chain direction, using $BaFe_2Se_4$ as an example. (c) Schematic crystal structure of $Ce_2O_2FeSe_2$ with space group Ibam (No. 72) in the conventional cell (blue, Ce; red, O; brown, Fe; green, Se). (d) Schematic crystal structure of $AFeX_2$ (A = K or Rb; X = S or Se) with space group C2/c (No. 15) in the conventional cell (purple, K or Rb; brown, Fe; green, Se or S). (e) Schematic crystal structure of $TlFeX_2$ (X = S or Se) and $CsFeSe_2$ with space group C2/m (No. 12) in the conventional cell (purple, Tl; brown, Fe; green, Se or S). (f) Schematic crystal structure of $CsFeS_2$ with space group Immm (No. 71) in the conventional cell (purple, Cs; brown, Fe; green, S. All the crystal structures were visualized with the VESTA code [35].

diffraction experiments also found a strong AFM coupling along the chain direction [31,33] in these Fe^{3+} chains. As summarized in Table I, both Fe^{2+} ($3d^6$) and Fe^{3+} ($3d^5$) chain systems exhibit very similar crystal structures along the chain direction, suggesting potential similarities in their physical properties. However, they also have some differences. Considering the present studies on iron Q1D systems, several physical questions naturally arise. At intermediate couplings, could the OSMP regime be realized in the Fe^{3+} chain? What causes the different magnetic coupling along the chain direction for the Fe^{3+} and Fe^{2+} chains? Can a unified picture be established to understand magnetic correlations across different iron chain systems? Can superconductivity occur in an Fe^{3+} chain?

To address these questions, we comprehensively study an Fe^{3+} chalcogenide chain, using $BaFe_2Se_4$ as a model system, employing a combination of density functional theory (DFT) and DMRG methods. Our DFT results show that the five iron orbitals of $BaFe_2Se_4$ also display entangled bonding and antibonding characteristics between different orbitals with large interorbital hoppings, which is quite similar to the case discussed for the Fe^{2+} chain [37]. The three-orbital model DMRG calculations indicate a very robust AFM coupling along the iron chain in the Fe^{3+} system. At the intermediate electronic correlation U/W region, an interesting OSMP regime was also obtained in the Fe^{3+} chain with the coexistence of localized and itinerant electrons. By modifying the electronic density to $n = 4$ in our three-orbital electronic Hubbard model, corresponding to Fe^{2+}, using the hopping matrix and crystal-field splitting from our case, remarkably, we found an FM state. In addition, changing the hopping matrix and crystal field splitting to those of the Fe^{2+} chain, using the electronic density $n = 3$ (corresponding to the Fe^{3+}), we

TABLE I. Summary of key structural and magnetic properties of various iron-chain systems, including space groups, valences of iron, nearest-neighbor Fe–Fe distances (Å), Fe–X (X = S or Se) bond lengths, magnetic correlations along the iron chain, magnetic transition temperatures T^* (K) and magnetic moments (μ_B/Fe), as obtained from experimental studies.

Column	Space group	Valence	Fe–Fe	Fe–X	Magnetism	T^*	Magnetic moment
$BaFe_2Se_4$ [27,36]	I4/m	+3	2.742	2.349	AFM	310	2.09
$BaFe_2S_4$ [28]	I4/m	+3	2.646	2.218			
$Ce_2O_2FeSe_2$ [29,30]	Ibam	+2	2.850	2.447	FM	171	3.33
$KFeSe_2$ [31,33]	C2/c	+3	2.815	2.363/2.369	AFM	310	3
$KFeS_2$ [31,33]	C2/c	+3	2.698	2.231/2.237	AFM	250	2.43
$RbFeSe_2$ [31,33]	C2/c	+3	2.831	2.383/2.386	AFM	250	2.66
$RbFeS_2$ [31,33]	C2/c	+3	2.716	2.235/2.245	AFM	188	1.83
$CsFeSe_2$ [40]	C2/m	+3	2.806/2.838	2.356/2.366			
$TlFeSe_2$ [32,41]	C2/m	+3	2.737/2.753	2.344/2.355	AFM	290	2.1
$TlFeS_2$ [32,41]	C2/m	+3	2.641/2.663	2.257/2.295	AFM	196	1.85
$CsFeS_2$ [33,42]	Immm	+3	2.699/2.721	2.262/2.220	AFM		1.88

obtained an AFM state. These results supported the mechanism proposed by our previous study [37], indicating that the electronic density of iron is responsible for the different magnetic behaviors in Fe^{3+} and Fe^{2+} chains. Moreover, we do not observe a clear pairing tendency in the Fe^{3+} chain at both intermediate and strong electronic correlations, suggesting that superconductivity is unlikely to emerge in these systems, or that the superconducting transition temperature, if present, would be very low. In this case, our results clearly establish the similarities and differences between Fe^{2+} and Fe^{3+} iron chains, in contrast to Fe^{2+} ladders.

II. METHODS

A. DFT method

To calculate the electronic structure of $BaFe_2Se_4$, first-principles DFT calculations were performed using the Vienna *Ab initio* Simulation Package (VASP), within the projector augmented wave (PAW) method [43–45]. The electronic correlations were considered by using the generalized gradient approximation (GGA) within the Perdew–Burke–Ernzerhof exchange-correlation potential [46]. Here, the plane-wave cutoff was set as 500 eV, and the k-point mesh was $8 \times 8 \times 12$ for the nonmagnetic calculations. For the calculation of the density of states, the k-point mesh used was $12 \times 12 \times 16$. In addition to the standard DFT calculations, the maximally localized Wannier functions (MLWFs) method was employed to fit the Fe $3d$ bands and obtain hopping parameters and crystal-field splitting by using the WANNIER90 packages [47].

B. DMRG method

To study the three-orbital electronic Hubbard model discussed in Sec. III [see Eqs. (1) and (2)], we used the many-body DMRG method [48–50], where the DMRG + + computer package was employed [51]. In the present DMRG calculations, at least 1400 states were kept and up to 21 sweeps were performed during the finite-size algorithm evolution. In previous studies of the same three-orbital Hubbard model but for materials with different hoppings and crystal-field splittings, using the same value for the number of kept states was shown to provide a good description of the chain systems studied, considering the balance between the accuracy of physical quantities and computational costs [37,52,53]. In addition, an electronic filling $n = 3$ in the three orbitals was considered. Here, a chain cluster lattice geometry with open-boundary conditions (OBC) was used for different lengths L. The truncation error remained below 10^{-6} for the calculation of spin–spin correlation, spin structure factor, charge occupancy, charge fluctuation, and squared spin. Furthermore, different lengths L and states m were considered in the study of the pairing tendencies.

To help readers reproduce our results, an example input file and additional details of the input parameters are described in the Supplemental Material [54].

III. MODEL SYSTEM

A. DFT results of $BaFe_2Se_4$

First, we briefly present the DFT results for the representative material $BaFe_2Se_4$. Based on the experimental crystal structure [27], we investigated the electronic structures for the nonmagnetic state of $BaFe_2Se_4$. The DFT results clearly establish both the similarities and differences between the Fe^{3+} and Fe^{2+} iron-chain systems, arising from their structurally similar chain geometry.

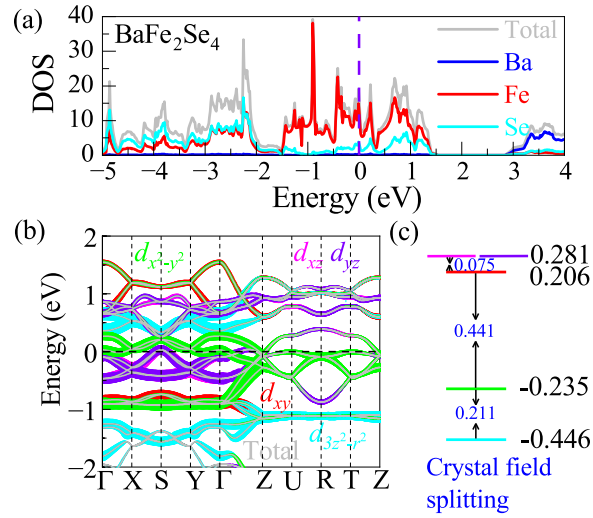

FIG. 2. (a) Density of states near the Fermi level of $BaFe_2Se_4$ for the nonmagnetic phase (gray, total; blue, Ba; red, Fe; cyan, Se). (b) Projected band structures of the nonmagnetic phase of $BaFe_2Se_4$. Note that the local $\{x, y, z\}$ axes of the projected orbitals correspond to crystal axes $\{a, b, c\}$, where the z axis is the c axis and the x or y axes are the a or b axes. The weight of each Fe orbital is represented by the size of the (barely visible) circles. (c) The crystal-field splitting energies of the five Fe $3d$ orbitals obtained by Wannier fitting. More details can be found in the Supplemental Material [54].

As shown in Fig. 2(a), the states near the Fermi level are mainly contributed by the Fe $3d$ orbitals hybridized with the Se $4p$ states. Furthermore, the Fe $3d$ bands of $BaFe_2Se_4$ are mainly located in the energy range from -1.5 to 1.5 eV, while the Se $4p$ bands are extended in real space. Compared with the bandwidth of the Fe $3d$ orbitals in the Fe^{2+} chain $Ce_2O_2FeSe_2$ system ($\sim$2.5 eV) [37], the Fe $3d$ bandwidth is slightly larger ($\sim$3 eV) for this Fe^{3+} iron chain, indicating a slightly enhanced nature of the itinerant behavior of the Fe $3d$ states in $BaFe_2Se_4$.

Furthermore, the reported spin magnetic moments for the Fe^{3+} chains range from approximately 1.8 to 3 μ_B/Fe, as displayed in Table I, which is significantly lower than the spin magnetic moment of the free Fe^{3+} ions ($\sim$5 μ_B/Fe). This behavior is quite common in the iron-based superconductors with FeX_4 tetrahedral coordination [55–57]. Using the local spin-density approximation (LSDA), which is widely applied in the DFT context of the Q1D and two-dimensional iron-based chalcogenides systems [5,24,55,58], we calculated that the local magnetic moment of Fe is about 2.82 μ_B/Fe. This value is also larger than the experimental value ($\sim$2.09 μ_B/Fe). This may be caused by the coexistence of localized Fe spins and itinerant electrons in the Q1D systems [57]. Another possible reason is that the quantum fluctuations are strong for the iron-based Q1D systems [55].

The DFT band structure of the nonmagnetic phase of $BaFe_2Se_4$ [see Fig. 2(b)] is more dispersive from Γ to Z

(parallel to the chains) along the chains than along other directions, such as Γ to X along the a axis. This anisotropy indicates a dominant QlD behavior along the k_z axis caused by the Q1D iron-chain lattice geometry. Similar to the case of $Ce_2O_2FeSe_2$ with $3d^6$ configuration, when interactions are neglected, the five iron orbitals of $BaFe_2Se_4$ also display entangled bonding and antibonding characteristics. In addition, we also obtained crystal-field splitting energies for the five iron $3d$ orbitals [54], based on the maximally localized Wannier functions [47], as displayed in Fig. 2(c), which are similar to those in the Fe^{2+} chain $Ce_2O_2FeSe_2$ [37]. Because of the similar $FeSe_2$ chain geometry in the Fe^{2+} and Fe^{3+} chains, the interorbital hoppings (nonzero off-diagonal matrix elements) are also found to be large in the case of $BaFe_2Se_4$ ($3d^5$). More Wannier-fitting results can be found in the Supplemental Material [54].

B. Model Hamiltonian

In the present study, as an example of an Fe^{3+} chalcogenide chain, we employ a canonical three-orbital Hubbard model defined on a 1D chain geometry, including the kinetic-energy and interaction terms given by $H = H_k + H_{\rm int}$. The tight-binding kinetic component is

$$H_k = \sum_{i\sigma\gamma\gamma'} t_{\gamma\gamma'}(c^\dagger_{i\sigma\gamma}c_{i+1\sigma\gamma'} + \text{H.c.}) + \sum_{i\gamma\sigma}\Delta_\gamma n_{i\gamma\sigma}, \qquad (1)$$

where the first term represents the hopping of an electron between orbitals γ at site i and orbitals γ' at the nearest-neighbor (NN) site $i+1$. $c^\dagger_{i\sigma\gamma}(c_{i\sigma\gamma})$ is the standard creation (annihilation) operator, γ and γ' indicate the different orbitals, and σ is the z-axis spin projection. Δ_γ denotes the crystal-field splittings of orbital γ.

The electronic-interaction portion of the Hamiltonian includes the standard intraorbital Hubbard repulsion U, the electronic repulsion U' between electrons in different orbitals, the Hund's coupling J_H, and the on-site interorbital electron-pair-hopping terms. Formally, it is written as

$$H_{\rm int} = U\sum_{i\gamma} n_{i\uparrow\gamma}n_{i\downarrow\gamma} + \left(U' - \frac{J_H}{2}\right)\sum_{\substack{i\\ \gamma<\gamma'}} n_{i\gamma}n_{i\gamma'} - 2J_H\sum_{\substack{i\\ \gamma<\gamma'}}\mathbf{S}_{i,\gamma}\cdot\mathbf{S}_{i,\gamma'} + J_H\sum_{\substack{i\\ \gamma<\gamma'}}(P^\dagger_{i\gamma}P_{i\gamma'} + \text{H.c.}), \qquad (2)$$

where the standard relation $U' = U - 2J_H$ is assumed, and the interorbital pair-hopping operator is $P_{i\gamma}{=}c_{i\downarrow\gamma}c_{i\uparrow\gamma}$.

Here, we consider a three-orbital Hubbard model with three electrons per site, corresponding to the iron valence Fe^{3+} ($3d^5$). In principle, for the Fe^{3+} chain materials with a $3d^5$ configuration, all five iron $3d$ orbitals contribute to the low-energy bands near the Fermi surface [see Fig. 2(b)]. However, in the DMRG calculations, five-orbital Hubbard-type models require significantly larger computing costs with more hoppings, crystal-field splittings, Hund's coupling, and Hubbard interactions because of the exponential increase in the local Hilbert space and substantial entanglement growth, which is impossible with our present computing resources. Thus, here we consider the three-orbital Hubbard model in our DMRG simulations, for both physical and computational considerations, following our previous study of iron chains and ladders with a similar edge-sharing FeX_4 tetrahedron structure [37,52,59]. The case $n = 4$ (four electrons in three orbitals), the typical electronic density used in iron superconductors where iron is in the Fe^{2+} valence state, corresponds to six electrons in five orbitals [52,59,60]. Thus, the Fe^{3+} chain discussed here corresponds to $n = 3$ in the three-orbital model. Note that the three-orbital model has been widely employed in theoretical studies of real iron-based superconducting systems, and multiple efforts have provided evidence that the three-orbital approximation gives a good description of the material's physical properties [20,37,59–61]. For example, in the Fe^{2+} iron ladder system $BaFe_2Se_3$, the three-orbital DMRG studies [20,59] successfully captured the essential physics of the block OSMP, providing a consistent description of the original experimental discoveries [13,14]. A similar situation arises in iron-chain systems. Our previous three-orbital DMRG work [37] on the Fe^{2+} chain compound $Ce_2O_2FeSe_2$ demonstrated excellent agreement between theory and experiment [30]. Furthermore, for the $Fe^{2.5+}$ iron-chain $K_3Fe_2Se_4$, our three-orbital model successfully reproduced the block-type magnetic order observed in neutron-scattering experiments [62]. Taken together, these examples support the conclusion that the three-orbital model captures the essential physics of Fe-based chain and ladder systems.

The crystal-field splitting and hopping matrix elements are obtained from $BaFe_2Se_4$, as a concrete example. The noninteracting tight-binding band structure along the chain direction, using the nearest-neighbor hopping matrix and crystal-field splitting obtained from $BaFe_2Se_4$, is displayed in Fig. 3(a), which qualitatively reproduces the corresponding DFT bands.

The hopping matrix for the three-orbital chain system is obtained from the MLWFs of $BaFe_2Se_4$ in orbital space as follows:

$$t_{\gamma\gamma'} = \begin{bmatrix} -0.457 & 0.045 & -0.495 \\ 0.045 & 0.224 & 0.107 \\ -0.495 & 0.107 & -0.439 \end{bmatrix}. \qquad (3)$$

The crystal field splitting of the three orbitals is chosen as $\Delta_0 = -0.446$, $\Delta_1 = -0.235$, and $\Delta_2 = 0.206$, all in eV units. The total kinetic energy bandwidth W is about 2.6 eV for the three-orbital model. All the parameters mentioned above, including the hopping matrix and crystal-field splittings, were discussed in Note II of the Supplemental Material [54].

C. Observables

To study the three-orbital 1D Hubbard model for varying U/W, several observables were measured using the DMRG many-body technique. Although we use a SU(2)-symmetric Hamiltonian model as defined in this work, we did not explicitly implement the SU(2) symmetry in the DMRG simulations. Instead, we implemented canonical DMRG with U(1) spin symmetry only, conserving the total S^z. It is well known that DMRG calculations based only on U(1), rather than

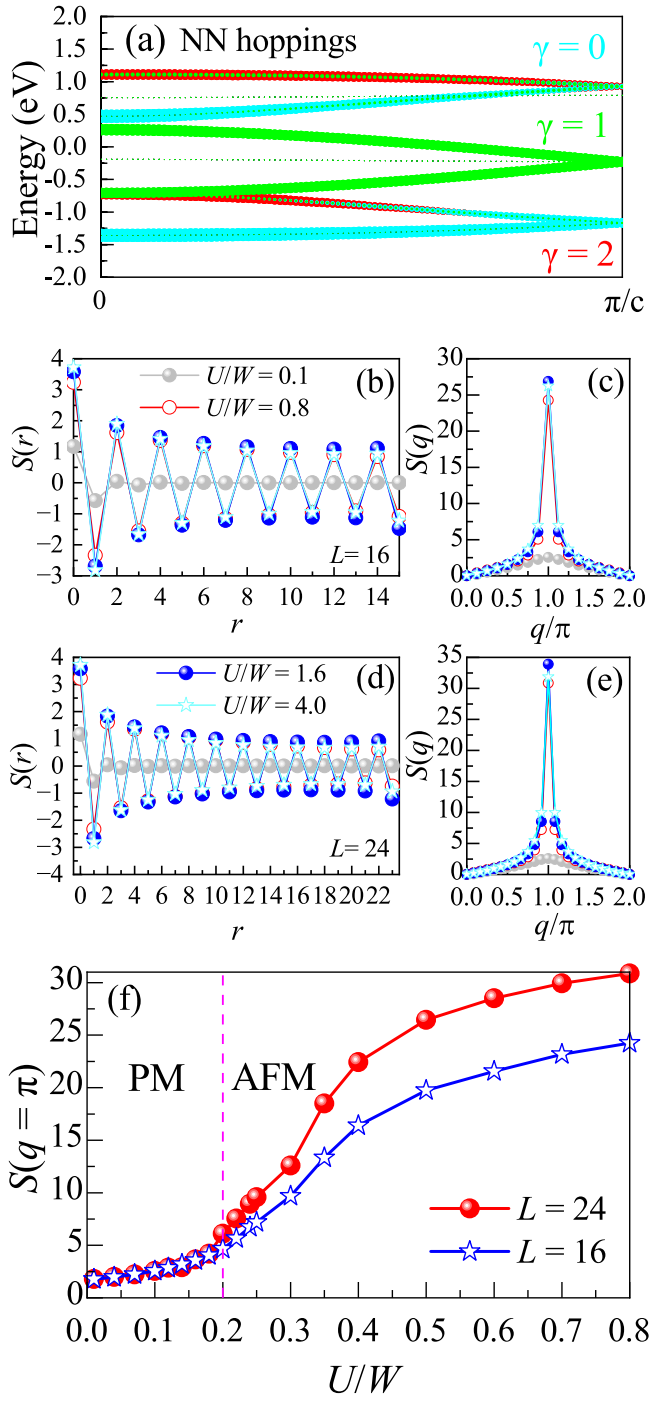

FIG. 3. (a) The noninteracting tight-binding band structure along the chain direction with nearest-neighbor hopping obtained from the example material $BaFe_2Se_4$. In this particular material ($BaFe_2Se_4$), there are two iron atoms in the chain, thus there are six bands in our tight-binding calculations. (b)(d) Spin–spin correlation $S(r) = \langle \mathbf{S}_i \cdot \mathbf{S}_j \rangle$ (with $r = |i - j|$ in real space). (c)(e) The spin structure factor $S(q)$ as a function of U/W at $J_H/U = 0.25$, respectively. Here, we use a chain lattice geometry with $L = 16$ and $L = 24$, respectively. (f) Spin structure factor $S(q = \pi)$ for different electronic correlations U/W and different lengths $L = 16$ and $L = 24$, respectively.

full SU(2), can describe ferromagnetic tendencies correctly. Within this framework, spin-up and spin-down sectors are treated explicitly on a U(1) basis. Accordingly, the number of kept states reported in this work refers to U(1)-symmetric bases, rather than SU(2) multiplet bases.

The spin–spin correlation is defined as

$$S(r) = \langle \mathbf{S}_i \cdot \mathbf{S}_j \rangle. \tag{4}$$

Here, $r = |i - j|$, and the spin at site i is

$$\mathbf{S}_i = \frac{1}{2} \sum_{\gamma} \sum_{\alpha\beta} c^{\dagger}_{i\gamma\alpha} \sigma_{\alpha\beta} c_{i\gamma\beta}, \tag{5}$$

where $\sigma_{\alpha\beta}$ are the matrix elements of the Pauli matrices.

The corresponding structure factor for spin is

$$S(q) = \frac{1}{L} \sum_{j,k} e^{-iq(j-k)} \langle \mathbf{S}_k \cdot \mathbf{S}_j \rangle. \tag{6}$$

The site-averaged occupancy of the orbitals is

$$n_{\gamma} = \frac{1}{L} \langle n_{i\gamma\sigma} \rangle. \tag{7}$$

The orbital-resolved charge fluctuation is defined as

$$\delta n_{\gamma} = \frac{1}{L} \sum_{i} \left(\langle n^2_{\gamma,i} \rangle - \langle n_{\gamma,i} \rangle^2 \right). \tag{8}$$

The mean value of the squared spin for each orbital is defined as

$$\langle \mathbf{S}^2 \rangle_{\gamma} = \frac{1}{L} \sum_{i} \langle \mathbf{S}_{i,\gamma} \cdot \mathbf{S}_{i,\gamma} \rangle. \tag{9}$$

While it is true that in 1D or Q1D systems, alternative nonmagnetic ordered phases, such as dimerized states, valence-bond-solid phases, and charge-density-wave states, can in principle emerge in certain parameter regimes, their existence should have appeared in our calculations. But they did not. Maybe by changing some model parameters, these competing phases may become relevant in some regions. But we employ hoppings and crystal-field splittings from DFT for the materials that are the focus of this work, and then solve the Kanamori-Hubbard multiorbital model within our best abilities via DMRG. Playing with the vast parameter space to discover additional phases is charming as an idea, but it is totally beyond the scope of the present work, which focuses on specific materials. DFT renders our work realistic for the materials of that are the focus of this work.

IV. DMRG CALCULATIONS

A. Spin–spin correlation

As shown in Fig. 3(b), the spin–spin correlation $S(r) = \langle \mathbf{S}_i \cdot \mathbf{S}_j \rangle$ decays rapidly as the distance r increases in the small Hubbard interaction U/W region (see $U/W = 0.1$ as an example), where the distance is defined as $r = |i - j|$, with i and j being site indices [63]. Accordingly, the spin structure factor $S(q)$ does not show an obvious peak in reciprocal space, indicating paramagnetic (PM) behavior. In this region, the kinetic term plays the leading role, resulting in a metallic PM state.

As U/W increases, the spin–spin correlation $S(r)$ increases at larger distances (see $U/W = 0.8$ case), as displayed in Fig. 3(b). In addition, the spin structure factor $S(q)$ also displays a sharp peak at $q = \pi$, indicating a staggered spin

pattern [see Fig. 3(c)]. Note that, eventually, at large distances, quantum fluctuations will prevent full long-range order in the one-dimensional model. Strictly in one-dimensional systems with continuous symmetry, as implied by the Lieb–Schultz–Mattis theorem, the spin–spin correlations eventually should decay slowly as a power law. In our results, although the strong spin correlations unveiled here resemble long-range order, in much larger systems the power-law decay will quite likely be observed. Moreover, we note that weak couplings between chains will stabilize the unveiled tendencies into long-range patterns with the canonical staggered antiferromagnetic order for the real material $BaFe_2Se_4$ system. Here, we do not make any claim of long-range order in one dimension in the paper. We focus on the *dominant tendencies*, which likely will become true long-range order after adding weak coupling between chains. This staggered spin pattern is also supported by DFT + U calculations for $BaFe_2Se_4$, as discussed in the Supplementa Material [54].

By further increasing U/W, we did not find any other magnetic pattern in the range of U/W ($U/W \leqslant 10$), indicating that the AFM coupling is robust along the chain direction [see Figs. 3(b) and 3(c)]. Furthermore, we also calculated $S(r)$ and $S(q)$ at larger L ($L = 24$), as displayed in Figs. 3(d) and 3(e), respectively. The results are similar to those for $L = 16$. Then, we conclude that the staggered AFM order is robust in the Fe^{3+} iron chain against changes in lattice length L. This conclusion is in good agreement with the present experimental results for $3d^5$ iron-chain systems: $BaFe_2Se_4$ [36], $AFeX_2$ (A = K or Rb and X = S or Se) [31], and $TlFeX_2$ (X = S or Se) [32]. This strong AFM coupling along the chain can be easily understood. In the half-filled multiorbital model, both intraorbital and interorbital hoppings favor the AFM coupling owing to the Pauli principle.

To better understand the PM–AFM phase transition in this system, we calculated the spin structure factor at $q = \pi$ for different values of U/W. Figure 3(f) clearly indicates a PM–AFM phase transition around $U/W = 0.2$ with a peak appearing in the spin structure factor $S(q)$, where the $S(q = \pi)$ begins to rapidly increase, indicating that AFM order forms. Furthermore, it should also be noticed that the specific boundary values of the PM–AFM phase transition are only a crude approximation, because finite-lattice-size effects and the use of a limited number of states in DMRG would affect the specific boundary values. In the present work, our purpose is not to provide a rigorous determination of the boundary of AFM correlations, but to determine the existence of the dominant phase regions.

B. Charge fluctuations

In addition, we calculated the site-averaged occupation number n_γ as a function of U/W at $J_H/U = 0.25$, as shown in Fig. 4(a). In the small-U/W region, $\gamma = 0$ and $\gamma = 2$ have noninteger n_γ values, indicating metallic behavior. As U/W increases, the occupation number of all orbitals converges to 1, leading to three half-occupied states, resulting in a Mott-insulator staggered AFM state.

Next, we also analyzed the charge fluctuations ($\delta n_\gamma = \frac{1}{L}\sum_i(\langle n_{\gamma,i}^2\rangle - \langle n_{\gamma,i}\rangle^2)$) for different orbitals, as displayed in Fig. 4(b). In the small-U/W region ($\lesssim 0.6$), the charge fluctuations for all three orbitals are considerable, indicating

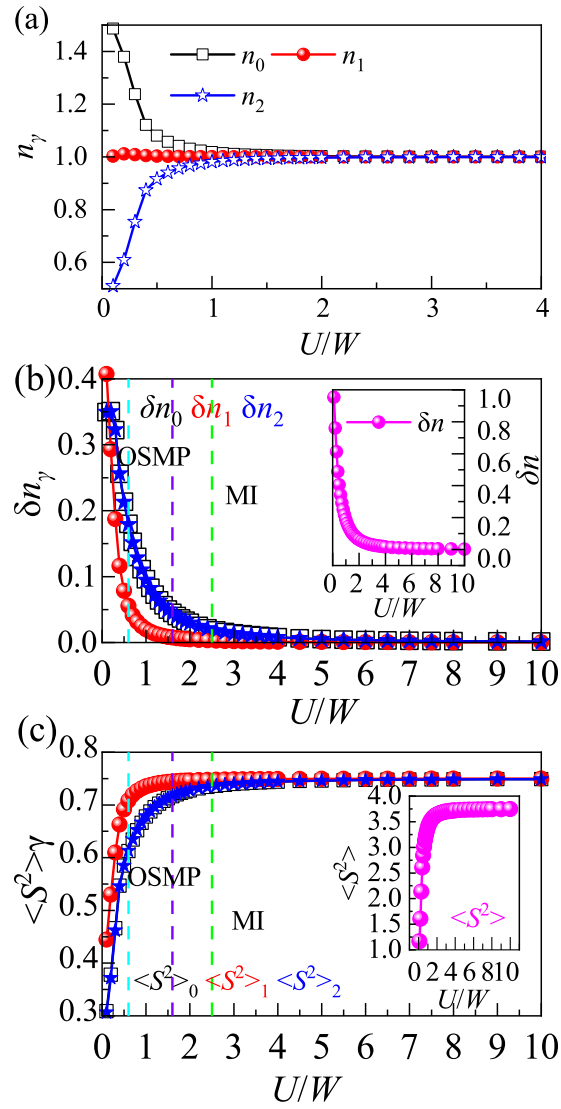

FIG. 4. (a) Orbital-resolved occupation number n_γ for different U/W, at $J_H/U = 0.25$. (b) Charge fluctuations $\delta n_\gamma = \frac{1}{L}\sum_i(\langle n_{\gamma,i}^2\rangle - \langle n_{\gamma,i}\rangle^2)$ for different orbitals as a function of U/W, at $J_H/U = 0.25$. Insert: total charge fluctuations $\delta n = \frac{1}{L}\sum_i(\langle n^2\rangle - \langle n\rangle^2)$. (c) The averaged value of the spin-squared $\langle S^2\rangle_\gamma$, for different orbitals, vs U/W, at $J_H/U = 0.25$. (Inset) The averaged value of the total spin-squared $\langle S^2\rangle$. Different phases are distinguished by the dashed lines with different colors. Here, our goal is to establish the dominant tendencies in the system. The phase boundaries of the OSMP and MI states are determined by the charge fluctuations of different orbitals, where the Mott insulator (MI) state is identified if there are no clear charge fluctuations. Note that these phase boundaries should be considered only as crude approximations. However, the existence of the different regions is clearly established even if the boundaries are only crude estimations. In addition, we used a lattice length $L = 24$.

strong quantum fluctuations along the chains, leading to a metallic state. The charge occupation of the $\gamma = 1$ orbital [see Fig. 4(a)] rapidly reaches 1 with only a slight change (~2%) around $U/W = 0.2$, but has sizable charge fluctuations in the small-U/W region. As U/W increases to intermediate Hubbard-coupling strengths, the charge fluctuations δn_1 rapidly reduces to nearly zero, resulting in localized-orbital

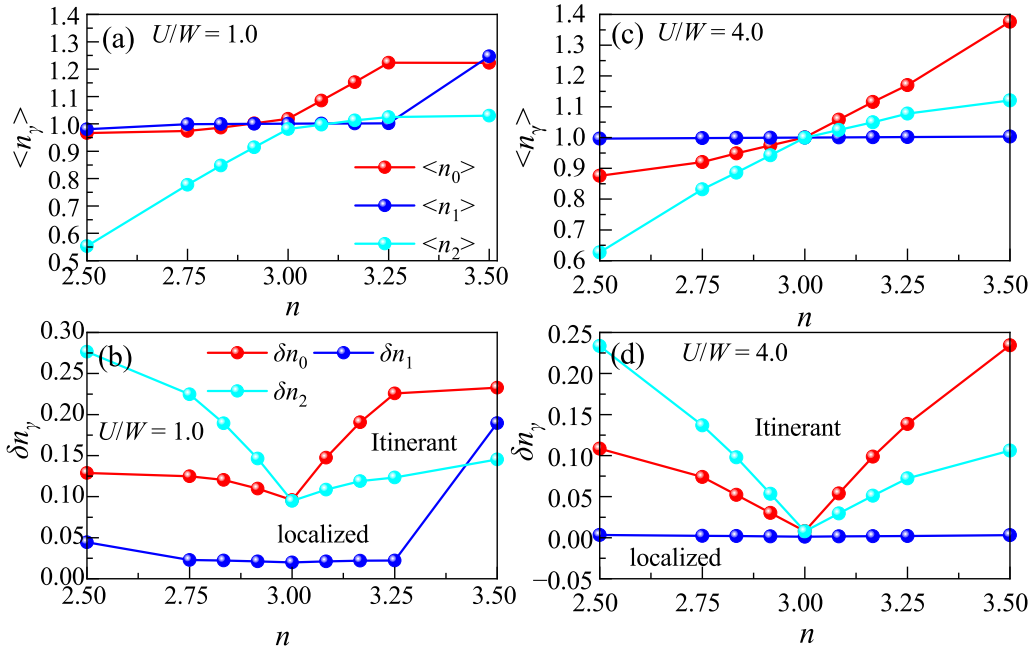

FIG. 5. (a) Orbital-resolved occupation number n_γ and (b) charge fluctuations δn_γ of the different orbitals as functions of doping at $U/W = 1.0$ and $J_H/U = 0.25$. (c) Orbital-resolved occupation number n_γ and (d) charge fluctuations δn_γ of different orbitals as functions of doping at $U/W = 4.0$ and $J_H/U = 0.25$. Here, we used a chain lattice of size $L = 24$. In (b) and (d), "localized" means that the orbital is Mott-localized ($\delta n_\gamma \sim 0$), and "itinerant" indicates that the orbital is metallic with sizable charge fluctuations.

characteristics. For comparison, the other two orbitals ($\gamma = 0$ and $\gamma = 2$) still retain sizable charge fluctuations, coexisting with itinerant-electron characteristics, leading to metallic orbital behavior. In this case, the system displays an OSMP in the intermediate-U/W regime ($\sim$0.6 to $\sim$1.6).

At even larger U/W ($\gtrsim$2.5), the charge fluctuations of all orbitals are reduced to nearly zero. Thus, the charge fluctuations are virtually suppressed by the electronic correlations. Consequently, this system displays insulating behavior in the strong-electronic-correlation region, as an AFM MI state with three half-filled orbitals ($\gamma = 0$, $\gamma = 1$, and $\gamma = 2$). As discussed in our previous study [53], the AFM–OSMP to AFM–MI transition is likely a "crossover" rather than a sharp, well-defined phase transition.

Furthermore, the calculated averaged value of the spin-squared of different orbitals also supports the above-described phase transitions, as shown in Fig. 4(c). In the small-U/W region, all the spin squared $\langle S^2\rangle_\gamma$ values are unsaturated for different orbitals. In the AFM OSMP region, $\langle S^2\rangle_1$ is saturated ($\sim$0.75), while $\langle S^2\rangle_0$ and $\langle S^2\rangle_2$ are still not fully converged to 0.75, indicating the presence of magnetic fluctuations. As we continue increasing U/W, eventually $\langle S^2\rangle_\gamma$ of all the orbitals saturates to 0.75, leading to a total $\langle S^2\rangle$ reaching 3.75 (three electrons in three orbitals), corresponding to the one-dimensional version of an AFM MI state.

We note that the phase boundaries should only be considered crude approximations, because finite-lattice-size effects and the use of a limited number of states in DMRG would affect the specific boundary values of this regime change from delocalized to localized electrons. However, although the lattice-size effects would affect the specific boundary values of the transitions, the existence of the different regimes is clear, even if the boundaries are only crude estimations.

Moreover, the interesting OSMP region was also reported in the Q1D iron ladder $BaFe_2Se_3$ [15,19,20], as well as in the Fe^{2+} iron-chain system $Ce_2O_2FeSe_2$ [38,39]. Hence, our results clearly indicate the similarity between Fe^{3+} and Fe^{2+} iron low-dimensional systems, with coexisting localized and itinerant electrons.

C. Orbital-selective Mott phase

To examine the stability of the OSMP, we also studied the occupation number and charge fluctuations for each orbital with different global filling numbers of electrons, for both intermediate and strong electronic correlations U/W, respectively. At intermediate electronic correlation, the system displays an OSMP with some charge fluctuations for the $\gamma = 0$ and $\gamma = 2$ orbitals [see the $n = 3.0$ results in Figs. 5(a) and 5(b)]. With hole doping, linear behavior was observed in the $\gamma = 0$ orbital with large charge fluctuations, while the $\gamma = 1$ orbital still retains Mott-localized characteristics. Furthermore, the occupation number of the $\gamma = 2$ orbital slightly changes containing some charge fluctuations under hole doping, as shown in Figs. 5(a) and 5(b). For electron doping, the $\gamma = 2$ orbital shows linear behavior with sizable charge fluctuations, while the $\gamma = 1$ orbital remains Mott-localized in some regions of electron doping. Thus, the OSMP can be stable in a wide range of doping at intermediate correlation.

For strong electronic correlations U/W, the $\gamma = 1$ orbital stays localized at both hole and electronic doping without charge fluctuations, as displayed in Figs. 5(c) and 5(d). Meanwhile, both the $\gamma = 0$ and $\gamma = 2$ orbitals display linear behavior under doping with fractional occupation, and thus metallic character, indicating a global OSMP behavior. Hence, all these results indicate that the OSMP physics could be

stable in both the intermediate and strong electronic correlation regimes. Our DMRG results suggest that the Fe^{3+} chain could also be quite interesting with OSMP physics involving the coexistence of localized and itinerant electrons, as widely discussed in the Fe^{2+} system [19–21,64,65]. Similar to the case of $BaFe_2Se_3$ [19], inelastic neutron scattering experiments could provide the key experimental evidence for the static and dynamic spin correlations involving the iron ions, which deserve further experimental efforts on $BaFe_2Se_3$ and related Fe^{3+} chains.

Here, we would like to note that our identification of the intermediate regime as an OSMP is primarily based on the orbital-selective behavior observed in the charge fluctuations, where one orbital shows strongly suppressed fluctuations while the others tremain relatively large. Thus, one behaves as an insulator while the other behaves as a metal. We acknowledge that this criterion alone is not fully conclusive in identifying an OSMP, but it is consistent with such an interpretation. A detailed dynamical spectral study of this region could provide stronger and better evidence for identifying the OSMP, such as discussed in Ref. [20] for the iron ladder $BaFe_2Se_3$. This computer-time-intensive calculation could be considered in future work.

D. Binding energy

Considering the pressure-induced superconductivity reported for the Q1D iron ladders $BaFe_2S_3$ [1] and $BaFe_2Se_3$ [2], here we also studied the binding energy of a pair of holes to explore the possibility of pairing tendencies in the Fe^{3+} chain, as defined in Refs. [66,67],

$$\Delta E = E(N-2) + E(N) - 2E(N-1), \tag{10}$$

where $E(N)$ is the ground-state energy of the N electron system for the three-orbital chain model. $E(N-2)$ and $E(N-1)$ are the ground-state energies of the two-hole doping or one-hole doping cases, respectively, corresponding to the $N-2$ and $N-1$ electron systems. If ΔE is found to be negative, it indicates possible pairing tendencies in this system, because the particles minimize their energy by creating a bound state. If ΔE is calculated to be positive, it means that the particles do not bind; thus, there are no pairing tendencies in the system. In this case and in the bulk limit, the doped holes would become two independent particles, leading to zero binding energy.

Based on the ground-state energies from DMRG calculations for the N (undoped case), $N-1$ (one hole), and $N-2$ (two holes) electron systems, we obtain the binding energy for different lengths L and states m, as shown in Fig. 6. At electronic correlation $U/W < 4$, the calculated values of ΔE are positive, indicating no pairing tendencies in this region for $L = 16$. In practice, the strong spin–spin correlations could obscure the emergence of pairing tendencies for a relatively small system size, such as $L = 16$. However, it would be very time-consuming to calculate spin and charge gaps for larger-scale systems in this region. Indeed, we tried finite-size scaling of the pairing gap binding energy at points using larger system sizes inside the region $U/W < 4$. The results were inconclusive, and we cannot rule out a tiny negative binding energy. Those calculations are extremely computationally costly, and the results are not of high accuracy because of the

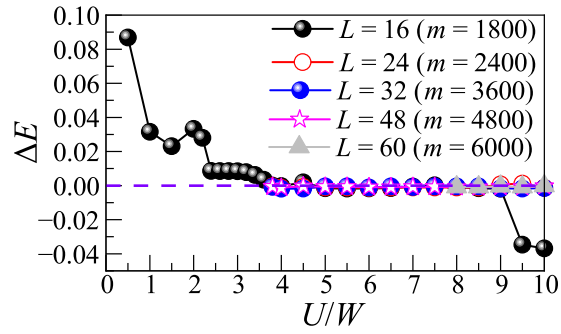

FIG. 6. The calculated binding energy vs electronic correlation strength U/W in a chain lattice for different lengths L and number of states m. Specifically, the maximal number of kept states was 1800, 2400, 3600, 4800, and 6000 for different lengths $L = 16$, 24, 36, 48, and 60, respectively. The truncation error is smaller than 10^{-6} everywhere except for the $L = 16$ data at $U/W < 3.8$. In the range 2.0–3.6, it is at least smaller than 10^{-5}. Because the DMRG computational cost is significantly higher in the region of small U/W, we only focused on the large-U/W points when using systems with larger sizes and more states. Here, the results were obtained at $J_H/U = 0.25$.

computational constraints of our computing resources. Thus, more convincing finite-size scaling is postponed to future work. For comparison, using the same method, our previous efforts found a strong pairing tendency for the Fe^{2+} ladders at a broad electronic-coupling U/W regime from ∼1 to ∼4 [66,67]. In this case, different from Fe^{2+} ladders, the Fe^{3+} case appears far from exhibiting pairing, and thus tendencies toward superconductivity, at least under the same conditions as those of iron ladders.

Furthermore, while at large U/W (>4), the calculated binding energies become slightly negative, their magnitude remains extremely small on the order of 10^{-4} eV, suggesting either the absence of pairing tendencies or, at most, a very weak pairing effect that is likely not robust. At $L = 16$, we do see a considerable negative binding energy at very large U/W, as shown in Fig. 6, but it disappears as the length L increases, indicating that it is likely a finite-size artifact rather than a true signature of pairing. Considering the electronic correlation of iron-based superconductor is at the intermediate region [55,56,58], this suggests that Fe^{3+} chains are unlikely to be superconducting.

In addition, we also investigated spin (ΔE_s) and charge (ΔE_c) gaps for several large values of U/W (= 4, 6, 8, 10) using different lattice sizes L up to 60, as shown in Fig. 7. We also calculated binding energies. In this regime, finite-size scaling suggests either zero or tiny $\Delta E_s > 0$ and zero or tiny binding energies $\Delta E_b < 0$. Clearly, the charge gap is larger by several orders of magnitude ($\Delta E_c \gg \Delta E_s$, $\Delta E_c \gg |\Delta E_b|$). The large charge gap presumably means that charges are mostly localized and suggests an incompressible charge state. The very weak spin gap suggests that the ground state resembles more an AFM spin arrangement, with very low-energy spin excitations. The tiny binding energies we found suggest that pairing is very weak or that there is no pairing in this system.

Recently, a high-pressure study provides support to our conclusions, where possible superconductivity was reported

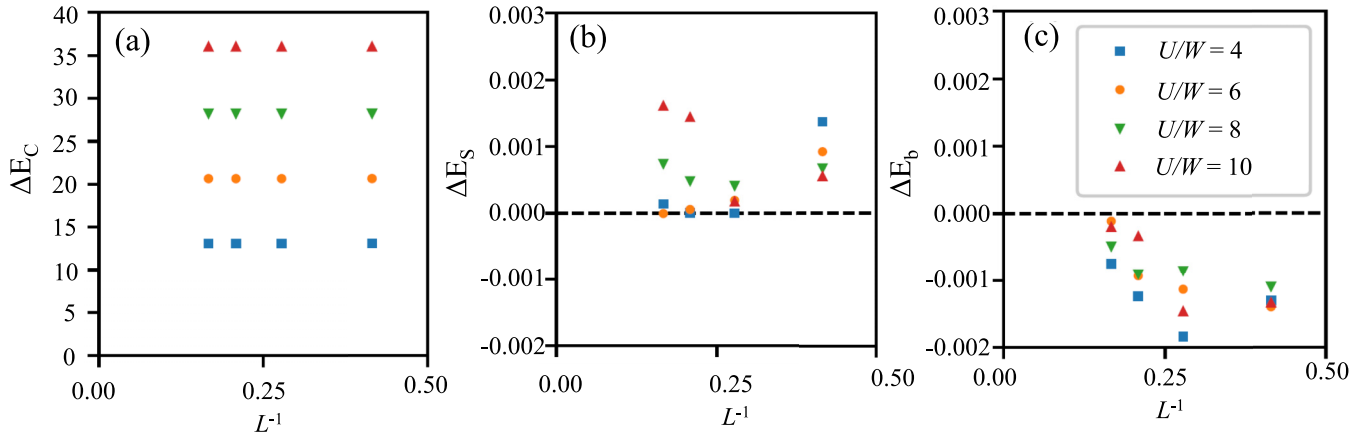

FIG. 7. The calculated (a) charge gap ΔE_c [$\Delta E_c = (E(N+1) + E(N-1) - 2E(N)]$, (b) spin gap ΔE_s [$\Delta E_s = E(S^z = 1) - E_0(S^z = 0)$, where $S^z = (N_\uparrow - N_\downarrow)/2$], and (c) binding energy ΔE_b [$\Delta E_b = E(N-2) + E(N) - 2E(N-1)$] parametric with electronic correlation strength U/W using a chain with different lengths L. Specifically, we use U/W equal to 4, 6, 8, and 10 for different lengths $L = 24$, 36, 48, and 60, respectively. All the results were obtained at $J_H/U = 0.25$.

but with a very low $T_C^{\text{onsite}} \sim 2$ K above 30 Gpa in the Fe^{3+} chain $TlFeSe_2$ [68]. A possible structural phase transition was also proposed $TlFeSe_2$ under pressure [68]. Then, the lattice and electronic properties could be changed substantially, depending on sample preparation and conditions. This requires a comprehensive DFT study for this Fe^{3+} chain or related chains to explore the possible lattice and electronic properties in high-pressure conditions. Based on the hoppings, crystal fields, and the relevant orbitals obtained from the high-pressure DFT study, a model calculation can provide more physical insight into the puzzle of high-pressure superconductivity in $TlFeSe_2$, as discussed in iron ladders [69–71]. All these issues deserve further theoretical investigation and discussion beyond the scope of our present paper.

E. Varying the electronic density

Recently, a half-full mechanism involving strong entanglement between doubly occupied and half-filled orbitals was proposed to explain the FM coupling along the chain direction in Fe^{2+} $Ce_2O_2FeSe_2$ [37]. To better understand this mechanism and to establish a connection between Fe^{3+} and Fe^{2+} chain systems, we now examine the magnetic correlations of our present model at an electronic filling of four electrons per site, corresponding to the Fe^{2+} valence.

At $U/W = 1$, different from the case of three electrons in three orbitals (AFM order already forms), Fig. 8(a) indicates that the spin–spin correlation $S(r)$ decays as the distance r increases, indicating PM behavior. This is caused by the competition between FM and AFM coupling, which are caused by interorbital and intraorbital couplings, respectively, at intermediate U/W. However, $S(r)$ also indicates the possibility of local short-range $\uparrow$ - $\downarrow$ - $\rightarrow$ order at $U/W = 1$. This is also supported by the calculated spin structure factor $S(q)$, where a small peak at $q = 2\pi/3$ was found, as displayed in Fig. 8(b). This magnetic phase ($\uparrow$ - $\downarrow$ - $\rightarrow$) is quite interesting, and deserves additional study by adjusting different parameters (electronic densities, hoppings, and crystal-field splitting) to stabilize this phase. However, we will not discuss further this possible phase, leaving that task for future work.

As U/W increases, the spin–spin correlation $S(r)$ gradually converges at larger distance, indicating FM tendency (see results for $U/W = 3$ or 6), as displayed in Fig. 8(a). Note that the approximately linear behavior of the FM spin–spin correlation as a function of distance r should not be interpreted as an intrinsic bulk scaling law. In general, FM spin–spin correlations are expected to saturate to a constant rather than exhibit a linear dependence on distance. The observed behavior arises from the combined effects of finite system size, OBC and the presence of strong ferromagnetic correlations in a finite chain. While larger system sizes would further reduce boundary effects, the purpose of Fig. 8(a) is not to extract the long-distance scaling form of the correlation function. Instead, it is intended to demonstrate the clear tendency toward ferromagnetic correlations along the chain and to illustrate the importance of electronic density in altering magnetism after introducing robust interorbital hopping. This FM tendency is unambiguously established by the data shown in Fig. 8(a), which is enough to support the conclusion that directly modifying the electronic density could alter the magnetic properties. The main message and conclusion discussed here do not depend on the shape of the curve. Furthermore, the spin structure factor $S(q)$ also displays a sharp peak at $q = 0$, corresponding to FM state [see Fig. 8(b)]. Thus, it suggests that the different magnetic coupling behaviors between Fe^{2+} and Fe^{3+} chains are caused by different electronic densities, where the orbital-selective character plays an important role. Hence, the results obtained by directly modifying the electronic density also support the notion that the half-full FM mechanism [37] is robust.

In addition, we also used a new set of hopping parameters and crystal-field splitting obtained from the Fe^{2+} chain [37] and changed the electronic density to 3 in the same model (corresponding to the Fe^{3+}),

$$t'_{\gamma\gamma'} = \begin{bmatrix} 0.187 & -0.054 & 0.020 \\ 0.054 & 0.351 & -0.349 \\ 0.020 & 0.349 & -0.433 \end{bmatrix}. \quad (11)$$

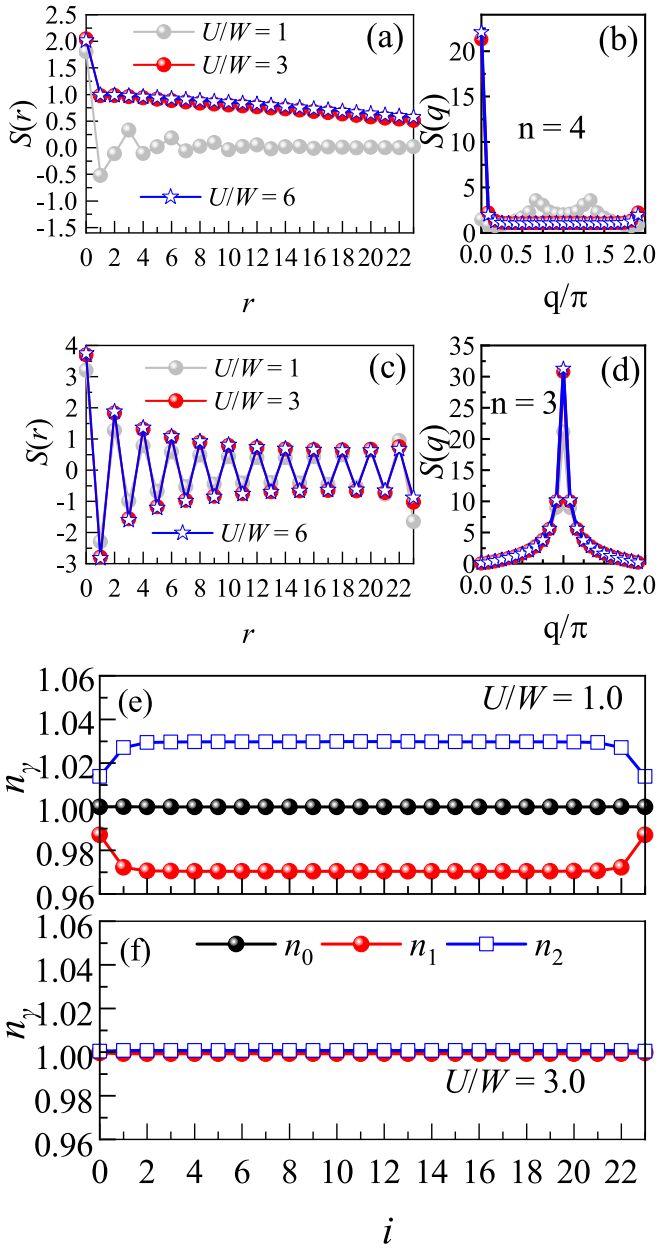

FIG. 8. (a) Spin–spin correlation $S(r)$ in real space, and (b) the spin structure factor $S(q)$, as a function of U/W, at $J_H/U = 0.25$, respectively, using the hopping matrix and crystal-field splitting obtained from $BaFe_2Se_4$. In (a) and (b), we use a chain lattice geometry with $L = 24$ and 96 electrons, corresponding to four electrons in three orbitals with 24 sites. (c) Spin–spin correlation $S(r)$ in real space, and (d) the spin structure factor $S(q)$, as a function of U/W, at $J_H/U = 0.25$, respectively, using the hopping matrix and crystal-field splitting obtained from the Fe^{2+} chain [37]. (c), (d) Orbital-resolved occupation number n_γ vs site i for both $U/W = 1$ and $U/W = 3$, respectively, at $J_H/U = 0.25$. (e), (f) Orbital-resolved occupation number n_γ for different sites at $U/W = 1$, and $U/W = 3$, respectively. Here, we use a chain lattice geometry with $L = 24$ and modify the number of electrons to 72, corresponding to three electrons in three orbitals with 24 sites.

The crystal-field splitting of the three orbitals are fixed at $\Delta_0' = -0.277$, $\Delta_1' = -0.203$ eV, and $\Delta_2' = -0.720$ eV, while the total kinetic energy bandwidth W' is 2.1 eV.

The spin–spin correlation $S(r)$ clearly shows AFM coupling along the chain for different U/W, as displayed in Fig. 8(c). Accordingly, the spin structure factor $S(q)$ also displays a sharp peak at $q = \pi$, indicating AFM state [see Fig. 8(d)]. In addition, we also studied the electronic occupation number of different orbitals n_γ for $U/W = 1$ and $U/W = 3$, respectively, as shown in Figs. 8(e) and 8(f). At $U/W = 1$, n_0 reaches 1 with nearly zero charge fluctuations while n_1 and n_2 are not quite close to 1, also with sizable charge fluctuations, leading to an OSMP. However, all three orbitals are half-filled with $n_\gamma = 1$ at $U/W = 1.0$, without charge fluctuations at $U/W = 3$, leading to MI phase. Note that in this set of hoppings, the large interorbital hopping is between γ_1 and γ_2 orbitals, while the γ_0 orbital has the smallest hopping. Hence, those qualitative similarities with the other set of parameters suggest that our physical conclusion regarding Fe^{3+} chain are solid and robust.

V. CONCLUSIONS AND DISCUSSION

Motivated by recent interesting developments in the study of low-dimensional 1D iron systems with $3d^6$ configuration (both two-leg ladders and chains), we investigated an iron-chain system with $3d^5$ configuration containing a FeX_4 (X = S or Se) tetrahedron block. To better understand the physics behind iron chains with $3d^5$ configuration, starting from $BaFe_2Se_4$, we comprehensively studied the electronic correlation effect in a three-orbital lattice model defined on a chain lattice by using DMRG many-body techniques. Our results establish the similarities and differences between Fe^{2+} and Fe^{3+} chains, as well as iron ladders.

Based on the electronic structures of the nonmagnetic phase of $BaFe_2Se_4$, the states near the Fermi level are mainly contributed by the Fe $3d$ orbitals hybridized with Se $4p$ orbitals. Similar to the case of $Ce_2O_2FeSe_2$ with Fe^{2+}, the five iron orbitals of $BaFe_2Se_4$ with Fe^{3+} also display entangled bonding and antibonding characteristics. Furthermore, the interorbital hoppings (nonzero off-diagonal matrix elements) are also found to be large in $BaFe_2Se_4$, as reported in $Ce_2O_2FeSe_2$ [37]. Because of their similar FeX_4 (X = S or Se) chain direction, the Fe^{3+} chains have similar electronic structures (see Note III of the Supplemental Material [54]), indicating similar physical properties in the Fe^{3+} chain systems.

In the range of U/W that we studied ($U/W \leqslant 10$), the spin–spin correlation $S(r)$ indicates an AFM coupling along the chain, corresponding to a sharp peak at $q = \pi$ in the spin structure factor $S(q)$. This agrees well with the present experimental results for the Fe^{3+} iron-chain systems. Recently, the large *interorbital* hopping between half-filled and fully occupied orbitals was proposed to explain the FM order in the Fe^{2+} iron-chain $Ce_2O_2FeSe_2$ [37]. Because of the similar 1D $FeSe_2$ chain structure, we also found a larger *interorbital* hopping in the Fe^{3+} chain case. By modifying the value of the electronic density to $n = 4$, corresponding to Fe^{2+}, using the hopping matrix and crystal field splitting from our case, we indeed found an FM state, supporting the mechanism proposed by our previous study [37]. In addition, using the hoppings from the $Ce_2O_2FeSe_2$ material [37] and changing the electronic density to $n = 4$ in our model, corresponding

to Fe^{3+}, we also obtained strong AFM order. This demonstrates that the magnetic structure, FM vs AFM, is controlled by the electronic density rather than by details of the band dispersion. On the other hand, the intraorbital hoppings lead to AFM tendencies; thus, the competition may lead to many interesting phases since electronic doping would enhance FM tendencies in the Fe^{2+} case. This competing aspect deserves further theoretical and experimental studies.

Our study also found an OSMP regime in the intermediate electronic correlation U/W region. Because the intraorbital hopping t_{11} (between $\gamma = 1$ orbitals) is much smaller than the others, the $\gamma = 1$ orbital is more easily Mott-localized at the intermediate Hubbard U region while the other two orbitals still remain metallic, leading to interesting AFM OSMP regime. The OSMP was also reported in the Fe^{2+} chain [37,39] and iron ladders [15,19,20]. This establishes interesting similarities between $3d^5$ and $3d^6$ iron low-dimensional systems. In addition, the OSMP with the coexistence of localized and itinerant electrons can also be stable under doping in both intermediate and strong electronic correlations. Considering the developments of OSMP low-dimensional iron systems with Fe^{2+}, the next interesting step is to study the dynamical excitations of this OSMP in the iron chain. We leave this task for future work.

Different from the strong pairing tendency in the typical electronic coupling U/W regime of Fe ($\sim$1 to $\sim$4) in $3d^6$ low-dimensional iron systems [66,67,71], in our study we do not observe any robust pairing tendency in the $3d^5$ iron chain by using the same model and method. Thus, it suggests that the pairing tendency, and associated superconductivity, will be difficult to stabilize in Fe^{3+} systems.

All the chains addressed here share a similar FeX_2 (X = S, Se, or Te) chain geometry built from edge-sharing FeX_4 tetrahedron blocks, leading to similar electronic structures. Although the specific values of hoppings and crystal-field splittings vary among those different chain materials, the key characteristics are the same: large *interorbital* hopping, while the values of the intraorbital hoppings vary greatly. Performing additional DMRG calculations for other iron-chain compounds with other parameter sets would substantially increase the computational cost, and this is beyond the scope of the current work. The specific values of the phase boundaries and the ranges of different phases would be different for other iron-chain materials because the Hamiltonian parameter sets would be different. However, we do not expect that the qualitative features of the phase diagram and the key physics will change in other Fe^{3+} chains. As discussed in our present work, the different magnetic properties of Fe^{2+} (ferromagnetism) and Fe^{3+} (antiferromagnetism) are controlled by the electronic density, related to the half-full interorbital mechanism [37]. Furthermore, the physical nature of the orbital-selective Mott phase is caused by varying intraorbital hoppings of different orbitals, where an orbital with smaller hopping could be Mott-localized at a smaller U, while one with larger hopping cannot be Mott-localized at the same U.

In summary, our study provides a starting point to connect the Fe^{3+} ($3d^5$) chains with other Fe^{2+} ($3d^6$) 1D systems. All our results indicate that the Fe^{3+} chain materials have interesting physics, although pairing is probably absent. Our work also establishes a unified picture to understand the different magnetic behaviors in Fe^{3+} ($3d^5$) and Fe^{2+} ($3d^6$) chains, as well as provides guidance for theoretical and experimental studies of the magnetism, OSMP, and superconductivity of iron chains.

ACKNOWLEDGMENTS

This work was supported by the U.S. Department of Energy, Office of Science, Basic Energy Sciences, Materials Sciences and Engineering Division. Parts of the finite-size-scaling computations for this work were performed on the high performance computing infrastructure operated by Research Support Solutions in the Division of IT at the University of Missouri, Columbia, MO [72]. This manuscript has been authored by UT-Battelle, LLC, under contract DE-AC05-00OR22725 with the US Department of Energy (DOE). The US government retains, and the publisher, by accepting the article for publication, acknowledges that the US government retains a nonexclusive, paid-up, irrevocable, worldwide license to publish or reproduce the published form of this manuscript, or allow others to do so, for US government purposes. DOE will provide public access to these results of federally sponsored research in accordance with the DOE Public Access Plan [73].

DATA AVAILABILITY

The dataset of the main findings of this study is openly available in the Zenodo Repository. In addition, the hopping and crystal field parameters for our DMRG calculations are available in this publication, and an example input file is also available in the Supplementary Material [54] and Zenodo Repository [74]. Furthermore, the *ab initio* DFT calculations are done with the code VASP. The DMRG code used in this study is available on GitHub [75].

[1] H. Takahashi, A. Sugimoto, Y. Nambu, T. Yamauchi, Y. Hirata, T. Kawakami, M. Avdeev, K. Matsubayashi, F. Du, C. Kawashima, *et al.*, Pressure-induced superconductivity in the iron-based ladder material $BaFe_2S_3$, Nat. Mater. **14**, 1008 (2015).

[2] J.-J. Ying, H. C. Lei, C. Petrovic, Y.-M. Xiao, and V.-V. Struzhkin, Interplay of magnetism and superconductivity in the compressed Fe-ladder compound $BaFe_2Se_3$, Phys. Rev. B **95**, 241109(R) (2017).

[3] T. Yamauchi, Y. Hirata, Y. Ueda, and K. Ohgushi, Pressure-induced Mott transition followed by a 24-K superconducting phase in $BaFe_2S_3$, Phys. Rev. Lett. **115**, 246402 (2015).

[4] Y. Zhang, L. F. Lin, J. J. Zhang, E. Dagotto, and S. Dong, Pressure-driven phase transition from antiferromagnetic semiconductor to nonmagnetic metal in the two-leg ladders AFe_2X_3 (A = Ba, K; X = S, Se), Phys. Rev. B **95**, 115154 (2017).

[5] L. Zheng, B. A. Frandsen, C. Wu, M. Yi, S. Wu, Q. Huang, E. Bourret-Courchesne, G. Simutis, R. Khasanov, D.-X. Yao, M. Wang, and R. J. Birgeneau, Gradual enhancement of stripe-type antiferromagnetism in the spin-ladder material $BaFe_2S_3$ under pressure, Phys. Rev. B **98**, 180402(R) (2018).

[6] S. Wu, J. Yin, T. Smart, A. Acharya, C. L. Bull, N. P. Funnell, T. R. Forrest, G. Simutis, R. Khasanov, S. K. Lewin, M. Wang, B. A. Frandsen, R. Jeanloz, and R. J. Birgeneau, Robust block magnetism in the spin ladder compound $BaFe_2Se_3$ under hydrostatic pressure, Phys. Rev. B **100**, 214511 (2019).

[7] Y. Zhang, L. F. Lin, A. Moreo, S. Dong, and E. Dagotto, Magnetic states of iron-based two-leg ladder tellurides, Phys. Rev. B **100**, 184419 (2019).

[8] J. M. Pizarro and E. Bascones, Strong electronic correlations and Fermi surface reconstruction in the quasi-one-dimensional iron superconductor $BaFe_2S_3$, Phys. Rev. Mater. **3**, 014801 (2019).

[9] H. Sun, X. Li, Y. Zhou, J. Yu, B. A. Frandsen, S. Wu, Z. Xu, S. Jiang, Q. Huang, E. Bourret-Courchesne, L. Sun, J. W. Lynn, R. J. Birgeneau, and M. Wang, Nonsuperconducting electronic ground state in pressurized $BaFe_2S_3$ and $BaFe_2S_{2.5}Se_{0.5}$, Phys. Rev. B **101**, 205129 (2020).

[10] W.-G. Zheng, V. Balédent, C. V. Colin, F. Damay, J.-P. Rueff, A. Forget, D. Colson, and P. Foury-Leylekian, Universal stripe order as a precursor of the superconducting phase in pressurized $BaFe_2Se_3$ spin ladder, Commun. Phys. **5**, 183 (2022).

[11] Y. Zhang, L. F. Lin, A. Moreo, S. Dong, and E. Dagotto, Iron telluride ladder compounds: Predicting the structural and magnetic properties of $BaFe_2Te_3$, Phys. Rev. B **101**, 144417 (2020)

[12] T. A. Maier and E. Dagotto, Coupled Hubbard ladders at weak coupling: Pairing and spin excitations, Phys. Rev. B **105**, 054512 (2022).

[13] J. M. Caron, J. R. Neilson, D. C. Miller, A. Llobet, and T. M. McQueen, Iron displacements and magnetoelastic coupling in the antiferromagnetic spin-ladder compound $BaFe_2Se_3$, Phys. Rev. B **84**, 180409(R) (2011).

[14] J. M. Caron, J. R. Neilson, D. C. Miller, K. Arpino, A. Llobet, and T. M. McQueen, Orbital-selective magnetism in the spin-ladder iron selenides $Ba_{1-x}K_xFe_2Se_3$, Phys. Rev. B **85**, 180405(R) (2012).

[15] J. Herbrych, J. Heverhagen, N. D. Patel, G. Alvarez, M. Daghofer, A. Moreo, and E. Dagotto, Novel magnetic block states in low-dimensional iron-based superconductors, Phys. Rev. Lett. **123**, 027203 (2019).

[16] J. Herbrych, J. Heverhagen, G. Alvarez, M. Daghofer, A. Moreo, and E. Dagotto, Block-spiral magnetism: An exotic type of frustrated order Proc, Proc. Natl. Acad. Sci. USA **117**, 16226 (2020)

[17] S. Dong, J.-M. Liu, and E. Dagotto, $BaFe_2Se_3$: A high T_C magnetic multiferroic with large ferrielectric polarization, Phys. Rev. Lett. **113**, 187204 (2014).

[18] T. Aoyama, S. Imaizumi, T. Togashi, Y. Sato, K. Hashizume, Y. Nambu, Y. Hirata, M. Matsubara, and K. Ohgushi, Polar state induced by block-type lattice distortions in $BaFe_2Se_3$ with quasi-one-dimensional ladder structure, Phys. Rev. B **99**, 241109(R) (2019).

[19] M. Mourigal, S. Wu, M. B. Stone, J. R. Neilson, J. M. Caron, T. M. McQueen, and C. L. Broholm, Block magnetic excitations in the orbitally selective Mott insulator $BaFe_2Se_3$, Phys. Rev. Lett. **115**, 047401 (2015).

[20] N. D. Patel, A. Nocera, G. Alvarez, A. Moreo, S. Johnston, and E. Dagotto, Fingerprints of an orbital-selective Mott phase in the block magnetic state of $BaFe_2Se_3$ ladders, Commun Phys. **2**, 64 (2019).

[21] L. Craco and S. Leoni, Pressure-induced orbital-selective metal from the Mott insulator $BaFe_2Se_3$, Phys. Rev. B **101**, 245133 (2020).

[22] E. A. Stepanov and S. Biermann, Can orbital-selective Néel transitions survive strong nonlocal electronic correlations? Phys. Rev. Lett. **132**, 226501 (2024).

[23] E. A. Stepanov, Eliminating orbital selectivity from the metal-insulator transition by strong magnetic fluctuations, Phys. Rev. Lett. **129**, 096404 (2022).

[24] Y. Zhang, L. F. Lin, J. J. Zhang, E. Dagotto, and S. Dong, Sequential structural and antiferromagnetic transitions in $BaFe_2Se_3$ under pressure, Phys. Rev. B **97**, 045119 (2018).

[25] P. Materne, W. Bi, J. Zhao, M. Y. Hu, M. L. Amigó, S. Seiro, S. Aswartham, B. Büchner, and E. E. Alp, Bandwidth controlled insulator-metal transition in $BaFe_2S_3$: A Mössbauer study under pressure, Phys. Rev. B **99**, 020505(R) (2019).

[26] K. Takubo, Y. Yokoyama, H. Wadati, S. Iwasaki, T. Mizokawa, T. Boyko, R. Sutarto, F. He, K. Hashizume, S. Imaizumi, T. Aoyama, Y. Imai, and K. Ohgushi, Orbital order and fluctuations in the two-leg ladder materials $BaFe_2X_3$ (X = S and Se) and $CsFe_2Se_3$, Phys. Rev. B **96**, 115157 (2017).

[27] D. Berthebaud, O. Perez, J. Tobola, D. Pelloquin, and A. Maignan, Crystal and electronic structures of two new iron selenides: $Ba_4Fe_3Se_{10}$ and $BaFe_2Se_4$, J. Solid State Chem. **230**, 293 (2015).

[28] J. S. Swinnea and H. Steinfink, The crystal structure of β-$BaFe_2S_4$: The first member in the infinitely adaptive series $Ba_p(Fe_2S_4)_q$, J. Solid State Chem. **32**, 329 (1980).

[29] E.-E. McCabe, D.-G. Free, and J.-S. Evans, A new iron oxyselenide $Ce_2O_2FeSe_2$: Synthesis and characterisation, Chem. Commun. **47**, 1261 (2011).

[30] E. E. McCabe, C. Stock, J. L. Bettis, M.-H. Whangbo, and J. S. O. Evans, Magnetism of the Fe^{2+} and Ce^{3+} sublattices in $Ce_2O_2FeSe_2$: A combined neutron powder diffraction, inelastic neutron scattering, and density functional study, Phys. Rev. B **90**, 235115 (2014).

[31] W. Bronger, A. Kyas, and P. Müller, The antiferromagnetic structures of $KFeS_2$, $RbFeS_2$, $KFeSe_2$, and $RbFeSe_2$ and the correlation between magnetic moments and crystal field calculations, J. Solid State Chem. **70**, 262 (1987).

[32] Z. Seidov, H.-A. Krug von Nidda, J. Hemberger, A. Loidl, G. Sultanov, E. Kerimova, and A. Panfilov, Magnetic susceptibility and ESR study of the covalent-chain antiferromagnets $TlFeS_2$ and $TlFeSe_2$, Phys. Rev. B **65**, 014433 (2001).

[33] Z. Seidov, H.-A. Krug von Nidda, V. Tsurkan, I. G. Filippova, A. Günther, T. P. Gavrilova, F. G. Vagizov, A. G. Kiiamov, L. R. Tagirov, and A. Loidl, Magnetic properties of the covalent chain antiferromagnet $RbFeSe_2$, Phys. Rev. B **94**, 134414 (2016).

[34] L. Li, L. Zheng, B. A. Frandsen, A. D. Christianson, D.-X. Yao, M. Wang, and R. J. Birgeneau, Spin dynamics of the spin-chain antiferromagnet $RbFeS_2$, Phys. Rev. B **104**, 224419 (2021).

[35] K. Momma and F. Izumi, *VESTA 3* for three-dimensional visualization of crystal, volumetric and morphology data, J. Appl. Cryst. **44**, 1272 (2011).

[36] X. Liu, K. M. Taddei, S. Li, W. Liu, N. Dhale, R. Kadado, D. Berman, C. D. Cruz, and B. Lv, Canted antiferromagnetism in

the quasi-one-dimensional iron chalcogenide $BaFe_2Se_4$, Phys. Rev. B **102**, 180403(R) (2020).
[37] L. F. Lin, Y. Zhang, G. Alvarez, A. Moreo, and E. Dagotto, Origin of insulating ferromagnetism in iron oxychalcogenide $Ce_2O_2FeSe_2$, Phys. Rev. Lett. **127**, 077204 (2021).
[38] L. F. Lin, Y. Zhang, G. Alvarez, M. A.McGuire, A. F. May, A. Moreo, E. Dagotto, Stability of the interorbital-hopping mechanism for ferromagnetism in multi-orbital Hubbard models, Commun. Phys. **6**, 199 (2023).
[39] L. F. Lin, Y. Zhang, G. Alvarez, J. Herbrych, A. Moreo, and E. Dagotto, Prediction of orbital-selective Mott phases and block magnetic states in the quasi-one-dimensional iron chain $Ce_2O_2FeSe_2$ under hole and electron doping, Phys. Rev. B **105**, 075119 (2022).
[40] P. Stüble and C. Röhr, $Cs[FeSe_2]Cs_3[FeSe_2]_2$, and $Cs_7[Fe_4Se_8]$: Missing links of known chalcogenido ferrate series, Z. Anorg. Allg. Chem. **643**, 1462 (2017).
[41] K. Klepp and H. Boller, Die kristallstruktur von $TlFeSe_2$ und $TlFeS_2$, Monatsh. Chem. **110**, 1045 (1979).
[42] Y. Ho, F. Nishi, C. F. Majkrzak, and L. Passell, Low temperature powder neutron diffraction studies of $CsFeS_2$, J. Phys. Soc. Jpn. **54**, 348 (1985).
[43] G. Kresse and J. Hafner, *Ab initio* molecular dynamics for liquid metals, Phys. Rev. B **47**, 558(R) (1993).
[44] G. Kresse and J. Furthmüller, Efficient iterative schemes for *ab initio* total-energy calculations using a plane-wave basis set, Phys. Rev. B **54**, 11169 (1996).
[45] P. E. Blöchl, Projector augmented-wave method, Phys. Rev. B **50**, 17953 (1994).
[46] J. P. Perdew, K. Burke, and M. Ernzerhof, Generalized gradient approximation made simple, Phys. Rev. Lett. **77**, 3865 (1996).
[47] A. A. Mostofi, J. R. Yates, Y. S. Lee, I. Souza, D. Vanderbilt, and N. Marzari, Wannier90: A tool for obtaining maximally-localised Wannier functions, Comput. Phys. Commun. **178**, 685 (2008).
[48] S.-R. White, Density matrix formulation for quantum renormalization groups, Phys. Rev. Lett. **69**, 2863 (1992).
[49] S.-R. White, Density-matrix algorithms for quantum renormalization groups, Phys. Rev. B **48**, 10345 (1993).
[50] U. Schollwöck, The density-matrix renormalization group, Rev. Mod. Phys. **77**, 259 (2005).
[51] G. Alvarez, The density matrix renormalization group for strongly correlated electron systems: A generic implementation, Comput. Phys. Commun. **180**, 1572 (2009).
[52] J. Rincon, A. Moreo, G. Alvarez, and E. Dagotto, Exotic magnetic order in the orbital-selective Mott regime of multi orbital systems, Phys. Rev. Lett. **112**, 106405 (2014).
[53] Y. Zhang, L.-F. Lin, G. Alvarez, A. Moreo, and E. Dagotto, Magnetic states of quasi-one-dimensional iron chalcogenide Ba_2FeS_3, Phys. Rev. B **104**, 125122 (2021).
[54] See Supplemental Material at http://link.aps.org/supplemental/10.1103/th25-rvx7 for additional methodological details and results, including the construction used to reproduce the DMRG results, Wannier function fitting, DFT calculations of other Fe^{3+} iron chains, and extended DMRG data.
[55] E. Dagotto, *Colloquium*: The unexpected properties of alkali metal iron selenide superconductors, Rev. Mod. Phys. **85**, 849 (2013).
[56] P. Dai, Antiferromagnetic order and spin dynamics in iron-based superconductors, Rev. Mod. Phys. **87**, 855 (2015).
[57] D. Ootsuki, N. L. Saini, F. Du, Y. Hirata, K. Ohgushi, Y. Ueda, and T. Mizokawa, Coexistence of localized and itinerant electrons in $BaFe_2X_3$ (X = S and Se) revealed by photoemission spectroscopy, Phys. Rev. B **91**, 014505 (2015).
[58] P. Dai, J. Hu, and E. Dagotto, Magnetism and its microscopic origin in iron-based high-temperature superconductors, Nat. Phys. **8**, 709 (2012).
[59] J. Herbrych, N. Kaushal, A. Nocera, G. Alvarez, A. Moreo, and E. Dagotto, Spin dynamics of the block orbital-selective Mott phase, Nat. Commun. **9**, 3736 (2018).
[60] M. Daghofer, A. Nicholson, A. Moreo, and E. Dagotto, Three orbital model for the iron-based superconductors, Phys. Rev. B **81**, 014511 (2010).
[61] Q. Luo, G. Martins, D.-X. Yao, M. Daghofer, R. Yu, A. Moreo, and E. Dagotto, Neutron and ARPES constraints on the couplings of the multiorbital Hubbard model for the iron pnictides, Phys. Rev. B **82**, 104508 (2010).
[62] F. Gao, N. Dhale, L.-F. Lin, K. M. Taddei, Y. Zhang, C. Dela Cruz, E. Dagotto, and B. Lv, Block-type antiferromagnetism in single chain quasi-one-dimensional $K_3Fe_2Se_4$, Phys. Rev. Lett. (2026), doi:10.1103/g8zx-gc2t.
[63] Regarding the choice of reference site, we just followed our previous DMRG studies on the one-dimensional chain or ladder systems by setting the leftmost edge as the reference site to calculate the spin–spin correlation from other sites j. However, the dominant underlying magnetic tendency remains unchanged if other conventions are used, as discussed in the Supplemental Material [54].
[64] M. N. Emilian, R. Yu, and Q. Si, Orbital-selective pairing and superconductivity in iron selenides, npj Quantum Mater. **2**, 24 (2017).
[65] L. Benfatto, B. Valenzuela, and L. Fanfarillo, Nematic pairing from orbital selective spin fluctuations in FeSe, npj Quantum Mater. **3**, 56 (2018).
[66] N. D. Patel, A. Nocera, G. Alvarez, R. Arita, A. Moreo, and E. Dagotto, Magnetic properties and pairing tendencies of the iron-based superconducting ladder $BaFe_2S_3$: Combined *ab initio* and density matrix renormalization group study, Phys. Rev. B **94**, 075119 (2016).
[67] N. D. Patel, A. Nocera, A. Moreo, and E. Dagotto, Pairing tendencies in a two-orbital Hubbard model in one dimension, Phys. Rev. B **96**, 024520 (2017).
[68] Z.-Y. Liu, Q.-X. Dong, P.-F. Shan, Y.-Y. Wang, J.-H. Dai, R. Jana, K.-Y. Chen, J.-P. Sun, B.-S. Wang, X.-H. Yu, *et al.*, Pressure-induced metallization and structural phase transition in the quasi-one-dimensional $TlFeSe_2$, Chin. Phys. Lett. **37**, 047102 (2020).
[69] R. Arita, H. Ikeda, S. Sakai, and M.-T. Suzuki, *Ab initio* down-folding study of the iron-based ladder superconductor $BaFe_2S_3$, Phys. Rev. B **92**, 054515 (2015).
[70] N. D. Patel, N. Kaushal, A. Nocera, G. Alvarez, and E. Dagotto, Emergence of superconductivity in doped multiorbital Hubbard chains, npj Quantum Mater. **5**, 27 (2020).
[71] B. Pandey R. Soni, L.-F. Lin, G. Alvarez, and E. Dagotto, Intertwined charge, spin, and pairing orders in doped iron ladders, Phys. Rev. B **103**, 214513 (2021).
[72] https://doi.org/10.32469/10355/97710.
[73] https://www.energy.gov/doe-public-access-plan.
[74] https://doi.org/10.5281/zenodo.20328081.
[75] https://g1257.github.io/dmrgPlusPlus/.